

# The Structure of the Lingo-1 Ectodomain, a Module Implicated in Central Nervous System Repair Inhibition\*

Received for publication, August 2, 2006, and in revised form, September 15, 2006. Published, JBC Papers in Press, September 27, 2006, DOI 10.1074/jbc.M607314200

Lidia Mosyak<sup>1,†</sup>, Andrew Wood<sup>2</sup>, Brian Dwyer<sup>3</sup>, Madhavan Buddha<sup>3</sup>, Mark Johnson<sup>3</sup>, Ann Aulabaugh<sup>1</sup>, Xiaotian Zhong<sup>1</sup>, Eleonora Presman<sup>1</sup>, Susan Benard<sup>1</sup>, Kerry Kelleher<sup>1</sup>, James Wilhelm<sup>1</sup>, Mark L. Stahl<sup>1</sup>, Ron Kriz<sup>2</sup>, Ying Gao<sup>3</sup>, Zixuan Cao<sup>3</sup>, Huai-Ping Ling<sup>3</sup>, Menelas N. Pangalos<sup>1</sup>, Frank S. Walsh<sup>1</sup>, and William S. Somers<sup>1,2</sup>

From <sup>1</sup>Wyeth Research, Cambridge, Massachusetts 02140, <sup>2</sup>Wyeth Research, Princeton, New Jersey 08852, <sup>3</sup>Wyeth Research, Pearl River, New York 10965, and <sup>4</sup>Wyeth Research, Collegeville, Pennsylvania 19426

Nogo receptor (NgR)-mediated control of axon growth relies on the central nervous system-specific type I transmembrane protein Lingo-1. Interactions between Lingo-1 and NgR, along with a complementary co-receptor, result in neurite and axonal collapse. In addition, the inhibitory role of Lingo-1 is particularly important in regulation of oligodendrocyte differentiation and myelination, suggesting that pharmacological modulation of Lingo-1 function could be a novel approach for nerve repair and remyelination therapies. Here we report on the crystal structure of the ligand-binding ectodomain of human Lingo-1 and show it has a bimodular, kinked structure composed of leucine-rich repeat (LRR) and immunoglobulin (Ig)-like modules. The structure, together with biophysical analysis of its solution properties, reveals that in the crystals and in solution Lingo-1 persistently associates with itself to form a stable tetramer and that it is its LRR-Ig-composite fold that drives such assembly. Specifically, in the crystal structure protomers of Lingo-1 associate in a ring-shaped tetramer, with each LRR domain filling an open cleft in the adjacent protomer. The tetramer buries a large surface area (9,200 Å<sup>2</sup>) and may serve as an efficient scaffold to simultaneously bind and assemble the NgR complex components during activation on a membrane. Potential functional binding sites that can be identified on the ectodomain surface, including the site of self-recognition, suggest a model for protein assembly on the membrane.

Injured neurons in mature organisms are unable to effectively regrow their axons after central nervous system damage. One of the many factors restricting axonal regeneration after injury is the growth-inhibiting components associated with damaged myelin. At least three of these components, Nogo-66, myelin-associated glycoprotein (MAG),<sup>3</sup> and oligodendrocyte

myelin glycoprotein, either individually or collectively, have been shown to be potent inhibitors of neurite outgrowth (1, 2). All three signal inhibition through the Nogo receptor complex, composed of the ligand-binding Nogo-66 receptor (NgR) and two complementary co-receptors p75 and Lingo-1 that act as a signal-transducing pair on an axon's cell membrane (3, 4). Although both NgR and the p75 nerve growth factor receptor have well documented roles in the context of myelin inhibition, reports exploring the role of Lingo-1 are more recent.

Human Lingo-1 is a central nervous system-specific transmembrane glycoprotein (Fig. 1) also known as LERN-1, which belongs to a larger family of LRR-Ig-containing proteins involved in central nervous system development and axonal growth (5). Its large extracellular or ectodomain is thought to be of functional importance in protein-protein recognition and is characterized by a tandem array of multiple LRRs and one Ig-like domain. The first studies examining the role of Lingo-1 demonstrated that in cultured neurons Lingo-1 directly associates with NgR and p75 and that whenever myelin-NgR/p75-mediated growth inhibition is observed, Lingo-1 is present, and is essential to this process (6). The functional capacity of the tripartite complex to launch the downstream RhoA-dependent signaling pathway that evokes the inhibition of neurite outgrowth has been reported. Of note is the finding that truncated Lingo-1 lacking the intracellular domain restores neurite outgrowth *in vitro* by interrupting the interaction of Lingo-1 with its binding partners. Direct physical interactions between the full-length Lingo-1 and either NgR or p75 have been reported, as have interactions of truncated soluble Lingo-1 with either NgR or p75 (6). More recently, our understanding of this inhibitory system has changed with the identification of yet another member of the Nogo receptor complex, designated TROY (7). The latter belongs to the same, tumor necrosis factor-receptor family as p75 but, unlike p75, is broadly expressed in adult neurons, where it can substitute for p75 in the signaling complex, allowing for RhoA activation and outgrowth inhibition in neurons lacking p75 (7, 8). The current model for myelin-mediated inhibition includes therefore an alternative signaling complex that involves NgR, Lingo-1, and TROY.

In addition to its expression on neurons, Lingo-1 is also

\* The costs of publication of this article were defrayed in part by the payment of page charges. This article must therefore be hereby marked "advertisement" in accordance with 18 U.S.C. Section 1734 solely to indicate this fact. The atomic coordinates and structure factors (code 2JDS) have been deposited in the Protein Data Bank, Research Collaboratory for Structural Bioinformatics, Rutgers University, New Brunswick, NJ (<http://www.rcsb.org/>).

<sup>1</sup> To whom correspondence may be addressed: Dept. of Chemical and Screening Sciences, Wyeth Research, 200 Cambridge Park Drive, Cambridge, MA 02140. Tel.: 617-665-5208; Fax: 617-665-8993; E-mail: lmosyak@wyeth.com.

<sup>2</sup> To whom correspondence may be addressed: Dept. of Chemical and Screening Sciences, Wyeth Research, 200 Cambridge Park Drive, Cambridge, MA 02140. Tel.: 617-665-5208; Fax: 617-665-8993; E-mail: wsomers@wyeth.com.

<sup>3</sup> The abbreviations used are: MAG, myelin-associated glycoprotein; NgR, Nogo

receptor; LRR, leucine-rich repeat; CHO, Chinese hamster ovary; Bis-Tris, 2-bis(2-hydroxyethyl)amino-2-(hydroxymethyl)propane-1,3-diol; r.m.s., root mean square; NCAM, neural cell adhesion molecule; SIRS, single isomorphous replacement with anomalous scattering.



FIGURE 1. Domain organization of Lingo-1. Schematic of the domain location of Lingo-1 showing the N-terminal LRR module in red (1–382; LRR-N and LRR-C label the N- and C-cap, respectively), the Ig1 domain in green (383–477), the stalk region in gray (478–516), and the transmembrane (TM) segment plus cytoplasmic (C7) C-terminal tail in blue (517–580). The circles represent the occupied N-linked glycosylation sites identified in the three-dimensional structure.

detected in oligodendrocytes (9). In this study, Lingo-1 was reported to be a negative regulator of oligodendrocyte maturation and myelination, exerting its function through a Fyn-RhoA pathway. Although a link to these signaling molecules is noteworthy in light of the fact that a role for Fyn/RhoA signaling has been reported in oligodendrocyte differentiation and myelination (10), the precise mechanism by which Lingo-1 signaling is initiated and the nature of protein-protein interactions involved remain largely unknown. Agonist and antagonist or null versions of Lingo-1 modulate the amount of functional Lingo-1 and hence its activity. Blockade of normal Lingo-1 activity, modeled either by introduction of exogenous Lingo-1 to oligodendrocyte-neuron cocultures or with knock-out mice lacking Lingo-1, not only permits outgrowth of oligodendrocyte processes, it also results in highly developed myelinated axons. These findings coupled with complementary gain-of-function results suggest that Lingo-1 inhibitory signaling could be one of the factors controlling central nervous system myelination. An interesting point in this respect is the recent evidence that myelin debris inhibits differentiation of oligodendrocyte precursors and that myelin could in fact be an underlying cause of impaired remyelination (11). Whether this mechanism is relevant to the Lingo-1 inhibitory action in oligodendrocytes is not known.

All these findings underline the importance and complexity of the molecular action of Lingo-1 and have stimulated much interest in this molecule as a promising therapeutic target, in particular for the treatment of diseases associated with myelin deficiencies, such as multiple sclerosis and leukodystrophies. Because development of therapeutics to block Lingo-1 specific interactions may lead to a new class of inhibitors, the atomic details of its ligand-recognition module should have an immediate impact on the discovery of such inhibitors. With this goal in view, we have produced recombinant soluble Lingo-1 protein, confirmed its biological and functional binding activity, and determined its ectodomain crystal structure to 2.7-Å resolution. The structure provides the first atomic insights into this new member of an apparently unique signaling protein family that contains both LRR and Ig-like domains in their extracellular region. Structural and solution characterization of this molecule reveal another important and previously not recognized concept, oligomerization of Lingo-1, which may relate to the proposed role of Lingo-1 in the central nervous system. The unique structure of this molecule defines its potential functional binding sites and should now provide a basis for further research that will address physiological relevance of these findings to central nervous system function.

## EXPERIMENTAL PROCEDURES

**Protein Expression and Purification**—An extracellular portion of human Lingo-1 was expressed in lectin-resistant CHO Lec 3.2.8.1 cells as a C-terminal 6-His-tagged protein (residues 1–549, signal sequence 1–33). The human Lingo-1-His was subcloned into pSMEG vector behind a murine cytomegalovirus promoter and verified by sequencing analysis. CHO cells were grown and maintained in a humidified incubator with 5% CO<sub>2</sub> at 37 °C. DNA transfection and large-scale production of conditioned cell culture media for Lec3.2.8.1 cells were performed as described previously (12). The media expressing Lingo-1-His was exchanged into a buffer of 1 M Tris, 100 mM NaCl, pH 8.0, to which a mixture of protease inhibitors (complete inhibitors from Roche Applied Science) was added. The protein was captured by nickel-nitrilotriacetic acid resin and then purified by gel-filtration chromatography (Superdex-200). Ngr 1D4 (residues 27–451) fused at the C terminus with the 10-amino acid 1D4 epitope tag was expressed in CHO-A2 cells using the honeybee meletin secretory leader, then purified from the media by anti-1D4 affinity chromatography followed by gel filtration.

**Neurite Outgrowth Assays**—96-well plates were coated with a thin layer of nitrocellulose (Bio-Rad) before incubating with Lingo-1-His or control IgG-Fc (R&D Systems) proteins in the presence of 2.5 µg/ml MAG-Fc (R&D Systems) at 4 °C overnight. Wells were subsequently coated with 17 µg/ml of poly-D-lysine (Sigma), followed by an incubation in Dulbecco's modified Eagle's medium containing 10% fetal bovine serum. Postnatal day 5 rat cerebellar granule neurons were dissociated and seeded at a density of  $1 \times 10^4$  cells per well. Cells were cultured for 18–20 h before being fixed with 4% paraformaldehyde and stained with a neuronal specific anti-β-tubulin antibody (Tuj1, Covance). The average of total neurite lengths from each neuron was quantitated by Cellomics' Neurite Outgrowth Bioapplication from at least 400 neurons per well, in triplicate wells per experiment. Results have been repeated independently for more than three times.

**Cell-based Binding Assays**—25,000 CHO-DUKX cells stably expressing Ngr and p75 were seeded overnight in 96-well plate and then incubated with various concentration of Lingo-1-His in Hanks' balanced salt buffer with 1% fetal bovine serum, 20 mM HEPES for 2 h at 37 °C. Alkaline phosphatase-conjugated anti-His IgG was added, and the mixture was incubated for another hour. Bound Lingo-1-His was detected by incubation with AttoPhos substrate (Promega) at 0.6 mg/ml for half an hour and read on Flex Station (emission: 440 nm, excitation: 560 nm).

**Biacore Experiments**—Surface plasmon resonance with BIAcore was used to determine the equilibrium dissociation constant ( $K_D$ ) between Ngr 1D4 and Lingo-1-His. Ngr 1D4 was immobilized onto a CM5 chip using amine-coupling chemistry. A titration series using 2-fold serial dilutions was performed with the analyte Lingo-1-His ranging in concentration from 10 to 0.039 µM. A  $K_D$  of ~1 µM was determined for the Ngr 1D4

## Oligomeric Ectodomains of Lingo-1

and Lingo-1-His interaction by steady-state equilibrium analysis using BiAevaluation 3.0.

**Crystallization.**—To obtain diffraction quality crystals, the 6-His tag and stalk region were removed by proteolytic treatment with chymotrypsin for 2 h at 18 °C. The cleaved Lingo-1 was further purified and analyzed by gel filtration, SDS-PAGE, and mass spectrometry (molecular mass ~66.4 kDa compared with a value of ~71.62 kDa obtained for Lingo-1-His). For crystallization, the protein was concentrated to 4–6 mg/ml in TBS (Tris-buffered saline, 50 mM Tris, pH 8.0, 150 mM NaCl). Crystals were obtained at 18 °C in hanging drops using 1.2–1.4 M  $(\text{NH}_4)_2\text{SO}_4$ , 0.1 M sodium citrate, pH 5.0, as a precipitant. The protein crystallized in two forms, with both forms found in the same crystallization droplets: I222, with two molecules per asymmetric unit and 74% solvent content, and P2<sub>1</sub>2<sub>1</sub>2, with four molecules per asymmetric unit and 73% solvent content. For data collection, crystals were gradually transferred from the mother liquor to the stabilizing cryoprotecting solution containing 2.9 M sodium malonate, pH 5.2. This solution, in which crystals were found to be stable over the period of several days and over the pH range 5–7, was used for crystal derivatization. A single derivative that allowed structure determination by the SIRAS method was obtained from crystals were soaked in 50 mM  $\text{K}_2\text{PtCl}_6$  and 2.9 M sodium malonate at pH 7.0 for 24 h. Prior to data collection, all crystals were flushed cooled under a nitrogen stream at 100 K.

**Data Collection, Phasing, and Refinement.**—Two data sets obtained from crystals of space group I222 were used for phase determination: the 3.5-Å native data set and the 3.6-Å data set for the platinum derivative, both measured in house with Saturn 920 CCD mounted on an FR-E  $\text{CuK}\alpha$  rotating anode source (Rigaku, Japan). The higher resolution native data set was collected to 2.7 Å at Advanced Photon Source beamline 22-ID of Southeast Regional Collaborative Access Team from a crystal that belongs to the P2<sub>1</sub>2<sub>1</sub>2 space group. All data were integrated and scaled with HKL2000 (13).

The initial positions of platinum atoms in the derivative crystal were located with SHELXD (2001 Bruker-AXS, XM, version 6.12) using anomalous differences of platinum atoms at the  $\text{CuK}\alpha$  edge. The input SAS coefficients were prepared with XPREF (2001 Bruker-AXS, version 6.12). Refinement of heavy-atom parameters, phase calculation, and density modification by SOLOMON, all were performed with SHARP (14) at 20–3.6-Å resolution, using both anomalous and isomorphous differences from the native and derivative data sets. The final 3.6-Å SIRAS maps produced with SHARP were of interpretable quality and revealed two Lingo-1 molecules in the asymmetric unit. SHARP phases were further improved by 2-fold NCS averaging and phase extension to 3.5 Å in DM (15). The resulting maps allowed us to build an initial, 90% complete (~85 residues) model with QUANTA. This model was then used for molecular replacement with the P2<sub>1</sub>2<sub>1</sub>2 data set to utilize the higher 2.7-Å resolution data. A clear solution for four molecules in the asymmetric unit was identified with PHASER (16). The I222 and P2<sub>1</sub>2<sub>1</sub>2 crystal forms share the same tetrameric packing, in which the tetramer can be built by replicating a dimer around the 2-fold axis. Subsequent rounds of rebuilding

and refinement against the 2.7-Å data set were done with COOT (17) and REFMAC (18).

The final model contains 4 protein molecules (residues A1–477, B3–475, C2–477, and D3–476), 39 N-acetylglucosamine and 12 mannose residues, and 310 water molecules. Residues 1–2 at the N termini of B, C, and D, 476–477 at the C termini of B and D, and residues D32–34 were not modeled into the structure due to the lack of adequate electron density, presumably because of disordering. Geometric analysis of the final refined structure performed with MolProbity (19) places 94% of all residues in favored regions and 0.16% as outliers. Statistics for data collection, phasing, and refinement are summarized in Table 1.

**Chemical Cross-linking.**—The solution state of Lingo-1 (residues 1–478) was analyzed by chemical cross-linking and dynamic light scattering, and of Lingo-1-His by analytical centrifugation. To achieve a substantial level of cross-linking, 50  $\mu\text{M}$  Lingo-1 in 50 mM Tris, pH 7.5, 150 mM NaCl was buffer exchanged with 50 mM Tris, pH 8.7, 150 mM NaCl using a desalting column. The buffer exchanged Lingo-1 at 50  $\mu\text{M}$  was incubated with 75  $\mu\text{M}$  glutaraldehyde at 18 °C for 2 h. Cross-linked Lingo-1 was purified away from glutaraldehyde by washing the mixture several times with 50 mM Tris, pH 7.5, 150 mM NaCl, followed by concentration of the protein using a Microcon. As a negative control, Lingo-1 in 50 mM Tris, pH 8.7, 150 mM NaCl was incubated at 18 °C for 2 h. Both these samples were run on 4–12% Bis-Tris SDS-PAGE gel and protein bands were visualized by Coomassie staining.

**Dynamic Light Scattering.**—The hydrodynamic radius of Lingo-1 was measured at various protein concentrations (ranged from 4 to 125  $\mu\text{M}$ ) using a DynaPro DLS instrument. Each protein sample was centrifuged at 13,000 rpm for 15 min to remove any particulates. The supernatant was transferred to a quartz cuvette, and 10–20 readings at 18 °C were averaged per sample.

**Analytical Ultracentrifugation.**—Sedimentation equilibrium experiments were performed on a Beckman XLI/XLA analytical ultracentrifuge at 20 °C at three different rotor speeds (9,000, 12,000, and 18,000 r.p.m.) and four concentrations (1.0, 5.8, 16.6, and 49.3  $\mu\text{M}$ ). Samples were loaded into six-channel (1.2-cm path length) carbon-Epon centerpieces in an An-50 Ti titanium rotor. Scans were recorded at 230, 250, and 280 nm with a 0.001-cm spacing and ten replicates per point, and equilibrium was judged to be achieved when there was no deviation between successive scans taken 3 h apart. Data were analyzed by nonlinear regression with WinNONLIN (20). The solvent density and viscosity were calculated with the program Sednterp (21). The data were fit to different associating models (monomer-dimer-trimer, monomer-dimer-trimer-tetramer, and monomer-dimer-tetramer). The residual, variance of the fit, and  $R_2$  were used to judge how well the data fit to the different models. Better fits were obtained for protein concentrations <50  $\mu\text{M}$ , and the best fit was for a monomer-dimer-tetramer equilibrium model. Association constants for monomer-dimer-tetramer equilibria obtained from WinNONLIN were converted from absorbance ( $K_{\text{obs}}$ ) to molar units ( $K_{\text{diss}}$ ) with the equation,  $K_{\text{diss}} = K_{\text{obs}}/(\epsilon l)$ , where  $l$  is the path length of the cell (1.2 cm),  $\epsilon$  is the molar extinction at the wavelength

monitored ( $23,120 \text{ M}^{-1} \text{ cm}^{-1}$  at 250 nm), and  $n$  is the oligomer size.

**Sequence Analysis**—The set of homologous Lingo-1 sequences was retrieved with a BLAST search from the publicly available protein data base UniProt (Swissprot, TrEMBL, and PIR). The ectodomain regions (amino acids 1–477) of Lingo-1 sequences (primary accession numbers: Q96FE5\_Human, Q9N008\_Macfa, Q5RDI4\_Ponpy, Q9D1T0\_Mouse, Q50L44\_Chick, and Q562A6\_Rat) were extracted, subsequently analyzed, and aligned by using FASTA (22).

**Graphics**—The figures were generated using COOT (17) and PyMol.<sup>4</sup>

## RESULTS AND DISCUSSION

**Functional Characterization and Structure Determination of Recombinant Lingo-1**—To obtain a homogeneous high mannose glycoform of the protein suitable for crystallography studies, the extracellular portion of glycosylated recombinant human Lingo-1 (amino acids 1–516, coding sequence 34–549, plus a C-terminal 6-histidine tag) was produced in lectin-resistant CHO Lec 3.2.8.1 cells and purified to homogeneity as described under "Experimental Procedures." The obtained recombinant Lingo-1-His was evaluated in a neurite outgrowth assay and examined for binding to its partners Ngr and p75. We first established that neurite outgrowth from cerebellar granule neurons can be inhibited by immobilized MAG-Fc but not control IgG-Fc and then showed that Lingo-1-His is able to completely reverse the MAG-induced neurite outgrowth inhibition (Fig. 2, A–C). The physical interaction of Lingo-1-His with Ngr- and p75-expressing CHO cells was demonstrated in a separate experiment (Fig. 2D). We also examined the interaction of the Lingo-1-His protein with Ngr *in vitro*, employing a surface plasmon resonance assay (Fig. 2E). The steady-state equilibrium analysis indicated that soluble Lingo-1-His maintained micromolar affinity binding ( $K_d \sim 1 \mu\text{M}$ ) to the immobilized soluble Ngr. Although the use of immobilized and truncated proteins may not accurately reflect the binding affinities of these proteins on the cell surface, these data confirm that Lingo-1 structural determinants required for recognition of Ngr are sufficiently contained within its ectodomain.

Crystallization of the full-length ectodomain of Lingo-1-His produced small weakly diffracting crystals. Cleavage of the His tag and stalk region prior to crystallization, so that the resultant ectodomain extended from residues 1 to 478, yielded two new crystal forms, the best of which (crystal form P2<sub>1</sub>, 2, 2) diffracted to 2.7-Å resolution. The quaternary arrangement of the protein is the same in both crystal forms analyzed. In the I222 crystal form, the dimer of dimers is crystallographic in nature, whereas in the P2<sub>1</sub>, 2, 2 form, the same configuration is generated by four independent Lingo-1 molecules in the asymmetric unit. Experimental phases were derived by single isomorphous replacement with anomalous scattering (SIRAS) followed by molecular averaging and solvent flattening. A complete model for the four molecules in the crystallographic asymmetric unit was built iteratively and refined to an  $R$ -value of 21.5% ( $R_{\text{free}} = 25.5\%$ ) at

2.7-Å resolution. A representative portion of the resultant electron density map is shown in Fig. 3A, and the summary of the data collection, phasing, and refinement statistics is given in Table 1. All four molecules adopt similar, but not identical, conformations; the root mean square (r.m.s.) deviations of 0.5–1.3 Å for C $\alpha$ -atoms are mainly due to some flexibility of the interdomain tilt angle and to differences in loop regions.

**Protomer Architecture**—Protomers of Lingo-1 fold into a two-module, kinked structure resembling a question mark (Fig. 3B). The N-terminal LRR module (residues 1–382) is an elongated, fairly deep arc with 15 parallel  $\beta$ -strands on the concave face and mostly irregular extended structures on the convex face. Overall, the canonical architecture of this module is most similar to that of the Ngr ectodomain (24, 25), except for appreciable differences in arc curvature and arc length (Fig. 3C). In total, there are twelve complete LRRs, 23–25 residues each, plus one partial repeat, which together create a classic right-handed super-helical array. Each LRR begins with a  $\beta$ -strand and loops back by virtue of the consensus 24-residue sequence repeat motif:  $\text{XL}^2\text{XXL}^5\text{XL}^7\text{XXN}^{10}\text{XL}^{12}\text{XXL}^{15}\text{XXXXF}^{20}\text{XXL}^{23}\text{X}$ , where X can be any amino acid; L are hydrophobic residues, preferentially Leu, but also Ile, Val, Met, Phe, or Thr; N are less conserved in nature and include mostly Asn, but also Cys, Asp, Leu, or Trp; F represents Phe or Leu. The consensus residues at the indicated positions make up the interior of the LRR domain. As in a number of other LRR-containing proteins, the hydrophobic core of the LRR structure is sheltered on both ends by cysteine-rich capping regions. The "N-cap" (residues 3–32) has two anti-parallel  $\beta$ -strands, with a short  $\beta$ -hairpin linker and two disulfide bridges at the base (Cys<sup>3</sup>–Cys<sup>9</sup> and Cys<sup>7</sup>–Cys<sup>18</sup>), an arrangement that is very close in structure to Ngr. The "C-cap" (residues 333–382), much like the one in Ngr, is all coiled and helical, with a long  $\alpha$ 1 helix on the back, short  $\alpha$ 2 on top and two disulfide linkages (Cys<sup>334</sup>–Cys<sup>357</sup> and Cys<sup>336</sup>–Cys<sup>382</sup>). Some unique features are, however, worth noting. One of them is the hydrophobic interior, which has a high occurrence of aromatic rings (Phe<sup>342</sup>, Phe<sup>350</sup>, Phe<sup>362</sup>, Phe<sup>368</sup>, Phe<sup>371</sup>, Tyr<sup>379</sup>, and Phe<sup>380</sup>). In addition, there is a short loop (residues 349–354), which is integrated into the concave LRR structure in a different way (such as shown in Fig. 3, B and C), with the apex C $\alpha$  (Arg<sup>357</sup>) bulging away from the  $\beta$ -sheet to the concave space ( $\sim 7 \text{ Å}$ ), a feature that is not seen in the corresponding segment of Ngr (Fig. 3C). Potential significance of this will be discussed below.

Immediately following the LRR module is a compact Ig module (residues 383–477), which belongs to the I1 subset of Ig domains (26, 27). The five-strand  $\beta$ -sheet (A', C, C', F, and G) is twisted and curved, with a noticeable recess on its CC'FG face, whereas the smaller  $\beta$ -sheet (A, B, D, and E) is rather flat. Other characteristics include a  $3_{10}$   $\alpha$ -helical turn and a pronounced kink, where the first  $\beta$ -strand is split in two (A and A'). A search of the PDB indicated high structural homology of the Ig1 module to the third, Ig3 module of the neural cell adhesion molecule (NCAM) (28). Superposition of the two modules (Fig. 3D) results in an r.m.s. deviation of 1.58 Å for the 88 C $\alpha$  pairs and  $\sim 30\%$  residue identity, with most differences occurring on the surface.

<sup>4</sup>W. L. Delano (2002) *The PyMOL Molecular Graphics System*, DeLano Scientific, San Carlos, CA.

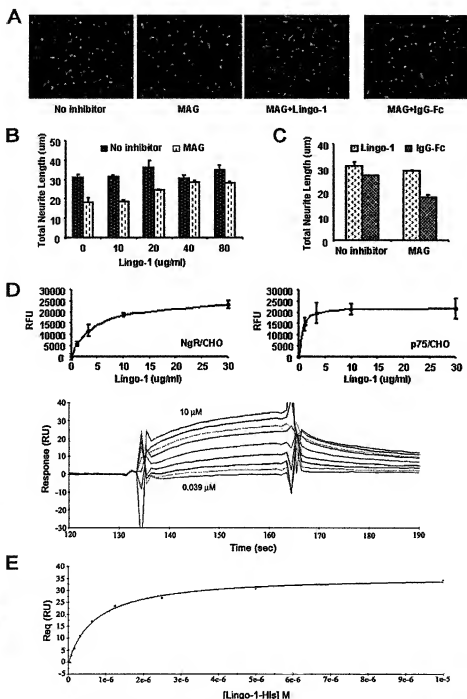


**FIGURE 2. Biological activity and functional characterization of recombinant Lingo-1.** **A** and **C**, block of neurite outgrowth inhibition induced by MAG (2.5 μg/ml) with Lingo-1 (40 μg/ml) but not with the control protein IgG-Fc of the same concentration. Neurite lengths were quantitated from >400 neurons/well in triplicate treatments. These results were repeated independently for more than three times. **B**, total neurite lengths from neurons cultured in the presence of MAG-Fc (2.5 μg/ml) were significantly increased by an application of Lingo-1 in a dose-dependent manner. **D**, Lingo-1 binding to CHO cells expressing either Ngr or p75. The data show the difference between transfected and non-transfected control. The values for half-maximal binding of Lingo-1 to Ngr and p75 were ~3 and 1 μg/ml, respectively. **E**, surface plasmon resonance evaluation of the interaction between Lingo-1-His and Ngr 1D4. Top, Biacore sensorgrams of a titration series with analyte Lingo-1-His and the immobilized Ngr 1D4 ligand. Binding curves are expressed as resonance units (RU) as a function of time. The experiments were performed in duplicate with one representative experiment shown. Lingo-1-His dissociation was allowed to proceed for 3 min returning to baseline between injections. The binding of Lingo-1-His to a reference surface was subtracted at each concentration of analyte examined. Bottom, a Biacore evaluation 3.0 fit of equilibrium binding response (*Req*) versus the concentration of Lingo-1-His. The steady-state affinity model was used to determine the equilibrium dissociation constant ( $K_D$ ).

A key feature of the ectodomain conformation is a sharp, close to 90° angle relating the LRR and Ig1 modules and placing the latter at the back, convex side of the LRR coil. Such topological arrangement allows for the formation of a wide, 22-Å deep and 35-Å long, cleft that extends on a glycan-free surface as if poised for binding. The sides of the cleft are formed from the convex and recessed faces of the two domains: namely the convex curvature of repeats 10–12 plus helix  $\alpha 1$  shapes one side and the concavity of the  $\beta$ -sheet A'CC'FG shapes the other. The opposed surfaces lie relatively far apart and have different chemical properties: the LRR face is polar and charged, whereas the CC'FG face is predominantly hydrophobic (Fig. 3B). Hence, the two modules appear not to interact with each other directly, except for few van der Waals contacts at the bottom cleft area. Of general note are the location of the Cys<sup>336</sup>–Cys<sup>382</sup> disulfide bond right at the tip of the elbow and the absence *per se* of an interdomain linker region. Cys<sup>382</sup> is the last residue in the C-cap, and Arg<sup>383</sup>, positioned immediately after, clearly belongs in the Ig1 domain (previously referred as to the basic region (6)). These features may constrain the positioning of the two modules relative to each other and to the membrane.

**Glycosylation**—The glycoform of Lingo-1 in lectin-resistant CHO cells is expected to be predominantly high mannose type glycans such as Man<sub>5</sub>GlcNAc<sub>6</sub>, which is consistent with mass spectrometry data (not shown). The sequence of the crystallized protein contains eight potential *N*-glycosylation consensus sites. Six of them are located in the LRR domain (Asn<sup>105</sup>, Asn<sup>163</sup>, Asn<sup>225</sup>, Asn<sup>235</sup>, Asn<sup>254</sup>, and Asn<sup>302</sup>) and two in the Ig1 domain (Asn<sup>453</sup> and Asn<sup>466</sup>). Of these eight predicted sites, all but one (Asn<sup>466</sup>) is found to be occupied. The putative site at Asn<sup>466</sup>-X-Ser<sup>468</sup>, located on the exterior A'CC'FG surface, is concluded unoccupied based on both the lack of electron density and

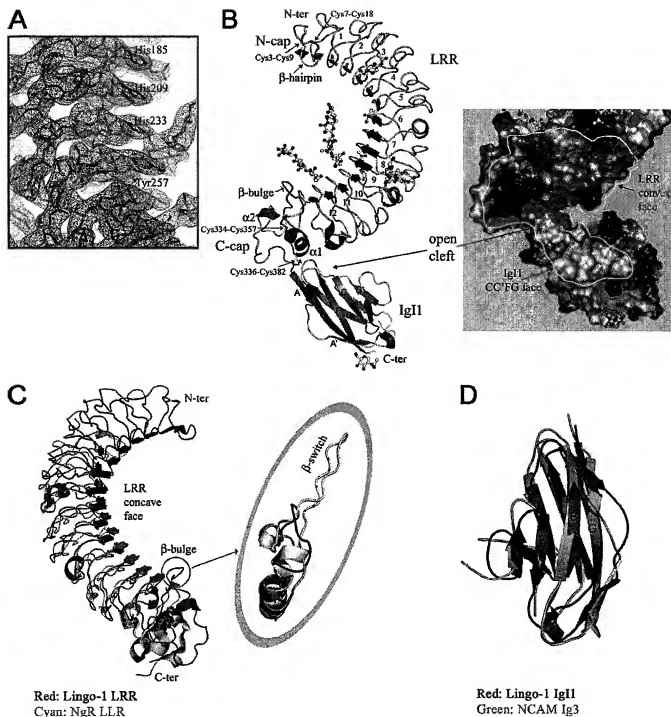


**FIGURE 3. The protomer structure of Lingo-1.** *A*, the  $2F_o - F_c$  electron density map (cyan mesh) is contoured at 1.3  $\sigma$  in the region of the His<sup>185</sup>–His<sup>209</sup>–His<sup>233</sup> ladder on the concave face of LRR (yellow stick model). *B*, side view. Ribbon diagram showing the overall architecture of the Lingo-1 monomer, colored according to secondary structure: beige, coil; blue,  $\beta$  strand; red,  $\alpha$  helix. Disulfide bonds are shown in green, and the N-linked carbohydrates are yellow. LRRs are numbered. Selected loops,  $\alpha$  helices, and  $\beta$  strands of the IgII domain are labeled. To the right is a close-up view of the cleft surface, marked with a white line and colored by electrostatic potential (red for negative; blue for positive) to emphasize different chemical properties of the opposed surfaces. *C*, superposition of the LRR structures of Lingo-1 (red) and NgR (cyan). Structures were aligned to highlight the difference in the C-cap regions. The small circle marks the location of the  $\beta$ -bulge in the Lingo-1 structure; its comparison to the segment of glycoprotein Gp1b $\alpha$  (yellow), discussed in the text, is shown to the right. *D*, superposition of the IgII module of Lingo-1 (red) with the Ig3 module of NCAM (green). The view is from the face of the  $\beta$  sheet ABDE.

on the observed interactions of Asn<sup>466</sup> in the intermolecular interface that is described in more detail later. The glycan cores at the remaining seven sites, for which densities can be assigned

unambiguously, are found throughout the structure as shown in Figs. 1 and 4. Remarkably, out of four LRR faces, only the convex surface is free of carbohydrate. By contrast, the concave

## Oligomeric Ectodomains of Lingo-1

TABLE 1

Crystallographic statistics for data collection, phasing, and refinement

| Data Collection                         | Native 1              | K2PtCl <sub>6</sub>            | Native 2               |
|---|-----------------------|--------------------------------|------------------------|
| Space Group                             | I222                  | I222                           | P21212                 |
| Unit Cell Dimensions                    |                       |                                |                        |
| a (Å)                                   | 148.7                 | 149.6                          | 201.5                  |
| b (Å)                                   | 158.6                 | 157.3                          | 149.7                  |
| c (Å)                                   | 200.0                 | 200.3                          | 157.5                  |
| Source                                  | FR-E CuK $\alpha$     | FR-E CuK $\alpha$              | APS ID-22              |
| Max. resolution (Å)                     | 3.5 (3.63-3.5)        | 3.6 (3.73-3.6)                 | 2.7 (2.8-2.7)          |
| Reflections (total/unique)              | 258,821/29,973        | 201,963/27,406                 | 913,490/129,431        |
| Completeness (%)                        | 98.2 (95.3)           | 98.9 (99.9)                    | 98.9 (94.7)            |
| Rsym <sup>a</sup> (%)                   | 12.6 (62.2)           | 11.9 (48.8)                    | 9.0 (61.9)             |
| I/ $\sigma$ (I)                         | 18.2 (3.2)            | 21.1 (4.7)                     | 21.5 (1.3)             |
| <b>Phasing</b>                          | <b>SIRAS</b>          | <b>Model Refinement</b>        | <b>Native 2</b>        |
| Anom. I/ $\sigma$ (I) (4.5Å /3.6Å)      | 2.3 /1.2              | Resolution (Å)                 | 50.0-2.7               |
| Riso <sup>b</sup> (%)                   | 43.6                  | Number of Reflections          | 122,982                |
| Rano <sup>b</sup> (%)                   | 8.6                   | Completeness (%)               | 98.7 (91.3)            |
| Number of Pt sites                      | 15                    | Rfactor/Rfree <sup>c</sup> (%) | 21.5/25.5              |
| Phasing Power <sup>c</sup> (4.5Å /3.6Å) | anomalous isomorphous | No. of protein atoms           | 15,114                 |
|   | 1.13 /0.6 1.1 /0.73   | No. of carbohydrate atoms      | 700                    |
| FOM <sup>d</sup> (4.5Å /3.6Å)           | 0.45 /0.25            | r.m.s. deviations              | bonds (Å) angles (deg) |
|   |                       |                                | 0.009 1.25             |

<sup>a</sup>  $R_{\text{sym}} = \sum_i \sum_j |I(h_i) - \langle I(h) \rangle| / \sum_i \sum_j I(h_i)$ , where  $\langle I(h) \rangle$  is the mean intensity. Numbers in parentheses reflect statistics for the highest resolution shells.<sup>b</sup>  $R_{\text{iso}} = \sum_i |F_{\text{obs}}(h_i) - F_{\text{calc}}(h_i)| / \sum_i F_{\text{calc}}(h_i)$  and  $R_{\text{ano}}$  is calculated for the amplitudes of the positive and negative counterparts of the Bijvoet pairs.<sup>c</sup> Phasing power is defined by  $(F(H)/\langle F(H) \rangle)$  (jack-of-closure), where  $H$  represents heavy-atom.<sup>d</sup> Mean figure of merit is the estimated mean cosine of the phase error.<sup>e</sup>  $R_{\text{free}}$  is calculated with 5% of the data.

and two major side surfaces are evenly glycosylated, each bearing two N-linked glycans. The last glycan maps to the A'CC'FG face of the IgL1 domain, but to the far membrane-proximal end of the domain, thereby rendering much of its surface still accessible.

In general, the presence of extensive glycosylation on glycoprotein surfaces limits their accessibility for interaction with ligands, and in most cases surfaces that are not covered with glycan chains are located where the ligands are predicted to bind. In most if not all LRR-related ligand complexes solved to date, the concave face of the LRR structure is essential for ligand-binding activities (29). In this regard, glycan decoration on the corresponding surface of Lingo-1 is quite unexpected though not unprecedented. The other LRR structure that revealed a high density glycosylation pattern on the concave face, which was otherwise thought to be a ligand-binding site, is that of human Toll-like receptor TLR3 (30).

To our knowledge, the role of glycosylation in Lingo-1 function has not been investigated. The importance and biochemical role of oligosaccharides in glycoproteins in general is well established, including protease protection, protein trafficking, folding, stability, and molecular geometry. In line with this, we found Lingo-1 to be consistently unstable upon deglycosylation *in vitro*, with a significant tendency to precipitate or aggregate over a wide pH range. Interestingly, of the seven occupied sites, two glycans that reside within the LRR concave  $\beta$  sheet may have an effect on the structure. As shown in Fig. 4, the glycan chain attached at Asn<sup>302</sup>, just one strand away from the begin-

ning of the C-cap, makes direct polar interactions with the residues of the aforementioned  $\beta$ -bulge (Arg<sup>352</sup> and Gln<sup>359</sup>) and appears well placed to contribute to its particular folding and positioning. The second carbohydrate, which comes from Asn<sup>254</sup>, faces toward the N-cap and following the curvature of the concave space fills the void of the central cavity, extending almost to the side of the N-terminal repeats.

**Tetramerization**—The structural relatedness of the two individual modules reflects directly on their ability to assemble into a high order tetramer, which we observe both in the crystals and by studies in solution. In the reported structure (crystal form P2<sub>1</sub>2<sub>1</sub>2), the four crystallographically unique Lingo-1 molecules wind around each other in a circular ring-like fashion to form a closed tetramer (Fig. 5A). The resultant structure has an approximate 4-fold axis of symmetry (C<sub>4</sub>) and approximate dimensions of 110 × 110 × 65 Å with a central hole of a diameter of ~45 Å. The four symmetrical partner molecules encircle the hole in a head-to-tail orientation, such that the N-terminal convex face of each LRR domain fills the opening of the ectodomain cleft on the next molecule. If we apply this geometry relative to a cell surface, then the protein rotation axis will lie approximately normal to the surface, the curved LRR domains will lie horizontally, back-to-back, whereas the IgL1 C-terminal ends will extend vertically as if to continue toward the membrane. To the best of our knowledge, such tetrameric assemblies have not been observed in LRR proteins before.

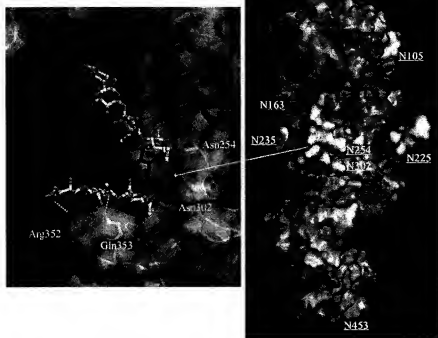


FIGURE 4. Glycosylation of Lingo-1, front view. The molecular surface of Lingo-1 is shown, colored according to electrostatic potential (red for negative, and blue for positive charges), with the surfaces represented in yellow for carbohydrate. The seven N-linked sugars are labeled. The back side of the molecule (not shown) is carbohydrate-free. The view on the left is tilted to highlight the position of the two N-glycans on the front concave LRR face. Hydrogen bonding is depicted with dashed white lines.

The observed mode of tetramerization yields four interfaces, all showing essentially the same geometry. The arrangement at each employs the bent cleft of one molecule as a binding site for another molecule (Fig. 5B), thus the packing of three surfaces: two from the cleft furnished as described above (C-terminal repeats 10–12, helix  $\alpha 1$ , and  $\beta$  sheet CC'FG) and one from the convex curvature of an adjacent monomer (N-terminal repeats 1–6). The convex-to-convex contacts provide half of the binding interface and primarily involve polar and charged residues. Sets of intricate hydrogen bonding (Fig. 5B, top) generate thirteen anchor points along the curve and contribute to the specificity of the interaction. Few van der Waals contacts (defined as  $<4$  Å) were also observed; the most prominent include a stacking interaction between Tyr<sup>290</sup> and Arg<sup>146'</sup> and close packing between Gly<sup>320</sup> and Tyr<sup>128'</sup>.

By contrast, the other half of the interface is largely through hydrophobic patches. The central elements of this interaction are four  $\beta$  strands C, C', F, and G and four consecutive back-loop regions of repeats 3–6 that curve along the opposing strands roughly following their directions. There are in total fourteen direct carbon-to-carbon contacts (Fig. 5B, bottom) and only two potential hydrogen bond contacts (Lys<sup>424</sup> N $\zeta$ –Asn<sup>163'</sup> O; Asn<sup>466</sup> N $\delta 2$ –Ile<sup>99'</sup> O). The potential glycosylation site Asn<sup>466</sup>–X–Ser<sup>468</sup> is part of the interface, contributing a fairly large surface area of interaction (Asn<sup>466</sup> has a total fractional accessibility index of 23%). Such important involvement is of apparent consequence: if it were utilized in the mature protein, glycosylation would cause a steric clash and prevent

binding of a partner molecule. Our solution studies indicate that the lack of glycosylation at this position is not an artifact of the mutant CHO cell line, because we were able to detect similar size tetramers with the Lingo-1 HEK cell-derived material (data not shown), a result that would be unlikely if this very site were glycosylated.

Tight packing requirements favor the presence of several glycine residues on both sides of the interface (positions 320, 464, 465, 74', 98', and 102'). Other details of this interaction include a few buried water molecules, the role of which is presumably to optimize the electrostatic complementarity of binding regions. Small differences in the ectodomain tilt angle ( $\sim 3^\circ$ ) suggest that the bound geometry of this interaction utilizes surfaces charge and hydrophobic complementarity as an efficient means of achieving both specificity and plasticity in binding. In general, the plastic nature of protein-protein interfaces is often identified as an emerging hallmark of surfaces of signaling

proteins and often cited as having a role in the mechanism of binding and release of signaling partners.

The many interactions between the two monomers bury a surface area of  $\sim 2,300$  Å<sup>2</sup>, comparable to and above the average size interface observed for protein-protein complexes in general ( $\sim 2,000$  Å<sup>2</sup> (31)). Accordingly, the total molecular surface area buried within the tetramer is  $\sim 9,200$  Å<sup>2</sup>. Comparable values have been found from studies of large tetrameric protein complexes ( $\sim 10,000$  Å<sup>2</sup> (32)). Such extensive contacts in the interface support the finding that Lingo-1 can exist as a tetramer. To explore the self-associating interactions of Lingo-1 in solution we employed chemical cross-linking, gel-filtration chromatography, dynamic light scattering, and analytical ultracentrifugation (Fig. 6). These experiments indicated that at concentrations  $>16$   $\mu$ M Lingo-1 is best modeled as a tetramer. Cross-linking of Lingo-1 with molar ratios of glutaraldehyde yielded a second band on a denaturing gel, with a molecular size expected for a tetramer  $\sim 260$  kDa (Fig. 6A). Upon gel filtration, Lingo-1 eluted as a single sharp peak with the retention time expected for a tetrameric species (200–300 kDa, Fig. 6B). Light scattering measurements showed that at concentrations of  $>16$   $\mu$ M the protein is predominantly in a single state (polydispersity of  $\sim 10\%$ ), with a hydrodynamic radius of 6.2 nm and a corresponding molecular mass of  $\sim 260$  kDa (Fig. 6C). Sedimentation equilibrium analysis of Lingo-1-His, performed at four protein concentrations (1.58, 16.6, and 49.3  $\mu$ M), indicated that at 16.6  $\mu$ M (Fig. 6D) Lingo-1 undergoes a monomer-dimer-tetramer self-association, with equilibrium association constants  $K_{1,2} \sim$



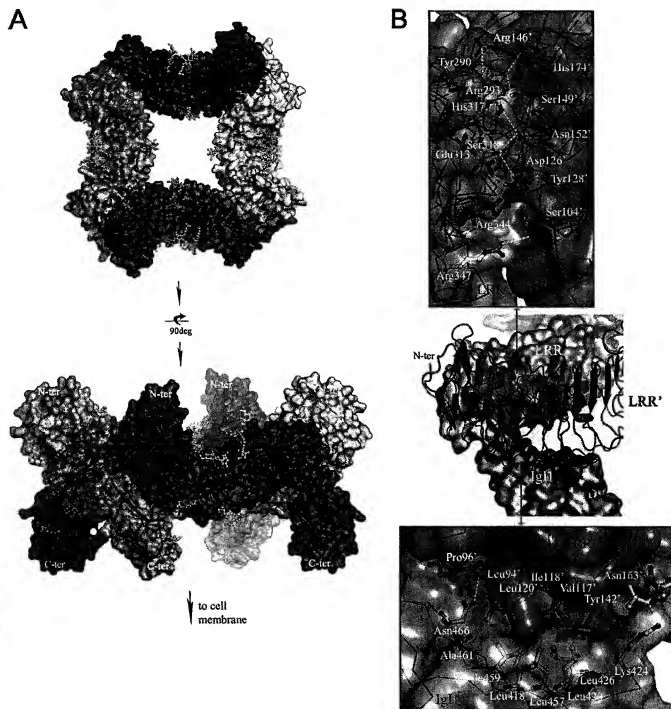


**FIGURE 5. Structure of the Lingo-1 tetramer.** A, view of the top and front surfaces of the Lingo-1 tetramer, rendered in red, green, magenta, and yellow. The two views are related by a 90° rotation about the horizontal axis. Carbohydrate are shown as yellow sticks. The LRR modules interlock the ring head-to-tail, back-to-back, with the IgTs extend vertically. The bottom view illustrates the putative orientation of the tetramer relative to a cell surface. B, detailed view of molecular interfaces. The imprint of bound LRR (red ribbons) on the molecular surface of a neighboring monomer is colored blue. The top and bottom insets are close-up views of some of the interactions at the LRR-LRR' and IgT-LRR' interfaces, respectively; the *prime* symbols denote the partner molecule. Molecular surfaces for the two interacting monomers are colored as in A, green and red. Side chains of interacting residues are shown as a ball-and-stick model, and hydrogen bonds are shown with dashed white lines. All interface residues are conserved apart from Ala<sup>461</sup> (Ser in chicken; see also Fig. 7A).

$2.65 \times 10^5 \text{ M}^{-1}$  and  $K_{2,4} \sim 5.020 \times 10^3 \text{ M}^{-1}$  for the monomer-dimer and dimer-tetramer steps, respectively. The stability of tetrameric species was examined during gel filtration, analytical centrifugation, and by light scattering. The tetrameric protein remained stable over a wide pH range and at a very low ionic

strength (data not shown). These studies, combined with the notion that similar tetrameric configurations are observed in two crystal forms (P2<sub>1</sub>2<sub>1</sub>2 and I222 symmetry), suggest that the formation of tetramers is not a consequence of crystal packing, but reflects tetramerization of Lingo-1 in solution.

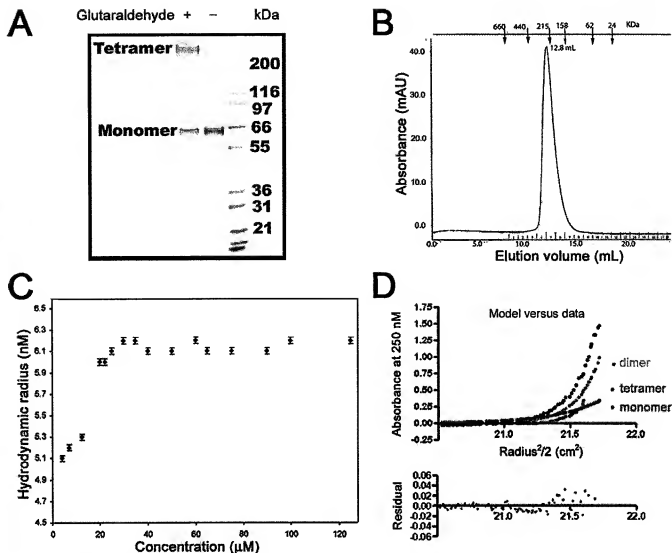


**FIGURE 6. Detection of Lingo-1 self-interaction by studies in solution.** A, cross-linking of Lingo-1 by glutaraldehyde. Shown is the SDS gel as visualized by Coomassie Blue staining. The gel contains the Lingo-1 control (lane 2) and 50  $\mu$ M Lingo-1 reacted with 75  $\mu$ M glutaraldehyde (lane 1). B, gel-filtration profile of Lingo-1. Fractions containing Lingo-1 are indicated (12.8 mL). C, apparent hydrodynamic radius of Lingo-1 measured by dynamic light scattering at concentrations of 4, 7, 12.5, 20, 22, 25, 30, 35, 40, 50, 60, 65, 75, 90, 100, and 125  $\mu$ M. D, sedimentation equilibrium analysis of Lingo-1 association. Shown are equilibrium sedimentation data obtained at 18,000 rpm, with a loading concentration of 16.6  $\mu$ M (blue circles) for a monomer-dimer-tetramer reversible equilibrium model. Residuals for the fit are shown beneath the graph. The purple, green, and red lines correspond to the relative proportions of monomer, dimer, and tetramer, respectively, calculated from the model.

**Classification of Possible Ligand Binding Sites**—The availability of the Lingo-1 structure may now facilitate a number of experiments, among which are site-directed mutagenesis and computational docking. To identify likely functional sites on Lingo-1, which could then help the strategies in future experiments, we analyzed its molecular structure in the context of both monomer and tetramer forms. This involved consideration of evolutionary conserved sequences, electrostatic surface potentials, carbohydrate exposure, and common characteristics that have emerged from the structures of other LRR- and Ig-related protein complexes.

Lingo-1 has a high degree of evolutionary conservation, with 92.7–99.8% extracellular sequence identity among human and homologous monkey, mouse, rat, and chicken (see “Experimental Procedures” for sequence accession information),

which suggest a precise biologically relevant function. The seventeen non-conservative mutations are shown in Fig. 7A. The remained conserved patterns, with much of the concave face, the self-recognition motifs, and glycosylation motifs, identify surfaces that may be important for ligand binding, oligomerization, or the structural integrity of folding topology.

Various studies have documented the key role of both electrostatic attraction and hydrophobic interaction upon protein-protein complexation (32). When the calculated electrostatic potentials are mapped on the molecular surface of Lingo-1, it becomes clear that tetramerization of Lingo-1 creates a large change in surface electrostatic potential (Fig. 7B, see also Fig. 4). This indicates a higher surface charge density and less hydrophobic nature for the tetrameric Lingo-1 molecules as compared with the monomeric molecules. The exposure of large

## Oligomeric Ectodomains of Lingo-1

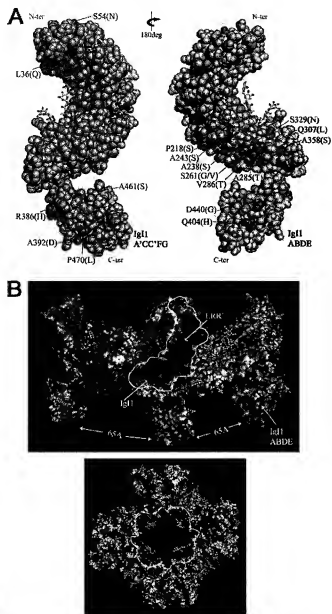


**FIGURE 7. Sequence conservation and electrostatic surface potential.** A, space-filling model showing the location of evolutionary mutations on the Lingo-1 structure. The two side views rotated 180° highlight residues that vary in red (labeled) and conserved in green. The highest amino acid sequence variations (human and chicken sequences; 92.7% identity) map to the convex area of LRR and some of the regions of the Ig1 domain. Substitutions that do not change the chemical or aromatic character of the amino acid (e.g. Arg to Lys, Ser to Thr, or Tyr to Phe) are not included. B, electrostatic potential of the tetramer. View of the front and top surfaces of the Lingo-1 tetramer, with coloring ranging from dark blue (most positive) to red (negative). White lines delineate composite surfaces, as discussed in the text: the V-shaped blue potential (combined from Ig1 and LRR) and the local positive potential inside the ring.

hydrophobic patches on a protein surface is in general energetically unfavorable, and such is the case with intact Lingo-1 monomers. Upon tetramerization, ~4000 Å<sup>2</sup> of hydrophobic surface area become buried, which by itself can be a driving force for assembly. Although it is formally possible that the Lingo-1 self-recognition site could also correspond or overlap with its ligand binding sites, we feel that this is less likely.

Further, because the tetramer reveals relatively fewer solvent-exposed hydrophobic residues, the interaction between Lingo-1 and its non-self ligands would be expected to involve a significant electrostatic component. In this vein, we find that the charge distribution on the composite tetramer surface is more striking, leading to the concept that the specificity of Lingo-1 may be largely due to its oligomeric structure and not its individual binding sites. Specifically, a remarkably large area of continuous positive charge, which develops on the molecule front face, could constitute an essential binding site for acidic p75 or a still unidentified acidic protein. Fourteen basic residues combine here from two facing molecules (arginines and lysines; all conserved across the species analyzed) to give this surface a V-shaped positive potential (Fig. 7B). Another note of interest is a net positive potential of the interior of the ring, which is due to repetitive clusters of arginine and histidine residues.

Extrapolating from knowledge of structurally available LRR-ligand complexes (29), two other surfaces on Lingo-1, both unobscured in the tetramer, deserve special mention: the concave face of the LRR module and the ABDE face of the Ig1 module. Examples of the LRR-ligand complexes suggest that, perhaps for Lingo-1, too, binding with ligands occurs at or near the concave LRR  $\beta$  sheet. The degree of the  $\beta$ -sheet binding differs for different ligand-receptor pairs. At one extreme is the LRR  $\beta$ -sheet of internalin that on its own completely surrounds the ligand domain of human E-cadherin, hEC1 (33). Such intimate contacts cannot be made with the corresponding interior of Lingo-1, because it is filled with carbohydrate. At the other extreme is the LRR  $\beta$ -sheet of platelet receptor glycoprotein 1b $\alpha$ , Gp1b $\alpha$ , that has minimal interaction with the ligand von Willebrand factor A1 domain; instead, it binds it with the two insertions, the  $\beta$  finger and the long  $\beta$  switch (34). The latter is also involved in the Gp1b $\alpha$ -thrombin interaction (35). An insertion at this position, although only 6-residues long, is also present in Lingo-1 and corresponds to the aforementioned interhelical  $\beta$ -bulge (see Figs. 3C and 8A). Features that are centered around the  $\beta$ -bulge structure are a prominently exposed tryptophan (Trp<sup>346</sup>) and a forward protruding arginine (Arg<sup>352</sup>). The latter two residues seem appropriate to consider for possible binding epitopes, especially in light of the fact that amino acids, particularly tryptophan and arginine (also tyrosine), are known to be more frequently encountered in protein-protein recognition sites or sites that are defined as hot spot residues (36). Interestingly, from the four LRR faces, the concave face shows the most contrasting set of differently polarized patches (Fig. 8A). Among these, elements that may be of relevance to Lingo-1 binding activity are a conspicuous conserved histidine ladder and a continuous area of exceptionally negative charge (Fig. 8A), which comes mainly from glutamic, but also aspartic acids (nine in total, all strictly conserved), extending diagonally across the  $\beta$  sheet to the N-terminal  $\beta$ -hairpin (" $\beta$ -finger" in Gp1b $\alpha$ ).

Finally, the structure of the Ig-like module of Lingo-1 evokes comparison with that of the Ig3 module of NCAM. Because both Lingo-1 and NCAM are part of a larger integrated family of cell adhesion-modulating molecules, the topological similarity of the referred domains can be interpreted in terms of evo-

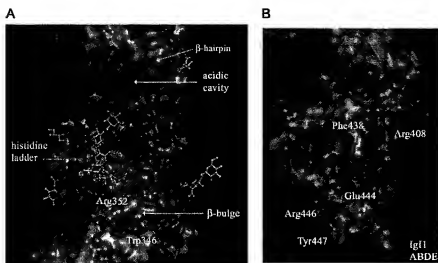


**FIGURE 8.** Selected features of the Lingo-1 structure. **A**, electrostatic potential surface of the concave LRR face showing a set of differently polarized patches and surface "hotspots." Regions that may represent sites of interaction with ligand are highlighted: the interhelical  $\beta$ -bulge (Tyr<sup>447</sup> and Arg<sup>446</sup>), the prominent acidic cavity (Glu<sup>444</sup>, Asp<sup>443</sup>, Asp<sup>442</sup>, Glu<sup>440</sup>, Glu<sup>438</sup>, Asp<sup>437</sup>, Glu<sup>436</sup>, and Glu<sup>435</sup>), and the histidine ladder (His<sup>435</sup>-His<sup>436</sup>-His<sup>437</sup>). **B**, surface diagram depicting electrostatic potentials of the solvent-facing ABDE sheet of the Ig1 module. Prominently exposed, conserved side chains, shown through the translucent surface, are labeled.

lutionary relationships. Although NCAM utilizes this general folding motif, namely the surface on its ABDE face, to mediate self-adhesive complexes on opposing cells (28), other members of this large family, such as cadherins, accomplish cell-cell adhesion by using a similar, though less closely related to Ig1, folding scheme. For instance, the hCE1 domain of E-cadherin, apart from being a docking site for *Listeria internalin*, is the primarily mediator of homotypic adhesion between epithelial cells (37, 33). In Lingo-1, the corresponding ABDE side on the Ig1 module is not involved in tetramer formation (Fig. 7B), rendering it available for other interactions and suggesting that this module, like that of LRR, may play an integrated role in oligomer formation and the recognition of a co-receptor. The probability of this, solely on the basis of topological homology, can be hard to assess but worth exploring, particularly in light of the precedence set by interactions between Ig-like and LRR domains of different molecules, as is the case with *internalin*/hCE1, *NgR*/MAG (38, 25), and now with Lingo-1/self. With this frame of reference, it is tempting to speculate that the *NgR* LRR may interact with the outward-facing surface of the Lingo-1 Ig1. The positions in this solvent-facing ABDE sheet are occupied by mostly charged, highly conserved residues (Fig. 8B), except for two (Gln<sup>404</sup> is substituted with histidine in chicken and Asp<sup>440</sup> is replaced by glycine in monkey, see also Fig. 7A). The spacing between the Ig1 domains in the tetramer (~65 Å between adjacent monomers; Fig. 7B) seems appropriate, allowing each to be competent to bind ligand.

**Concluding Remarks.**—The biological importance of Lingo-1 in central nervous system recognition and signaling events has only recently come to light. As a member of an emerging family of brain-enriched neuronal growth molecules and as part of the myelin-stimulated Nogo receptor complex, Lingo-1 has a demonstrated role in transducing *in vitro* processes of neurite inhibition and axonal collapse that likely relate to critical processes modulating regeneration occurring in the damaged brain. An

understanding of how this signaling is orchestrated is greatly hindered by the lack of structural information on the functional binding sites and the stoichiometry of the receptor complex. The Lingo-1 structural data described here revealed the unusual concept of an LRR protein tetramerization, which we further examined and confirmed by studies of Lingo-1 in solution. This unexpected architecture of Lingo-1 gives a framework for the design of experiments to address the biological relevance of oligomerization, and in particular, the still unresolved questions about the stoichiometry of the Lingo-1 receptor complex. Many studies on signaling-receptor proteins have shown evidence that oligomerization has a role in regulating receptor functions by influencing ligand binding and signaling properties (23). In its association with itself, Lingo-1 may provide a mechanism for assembly of the receptor complex components, localizing their signaling functions to the sites of neuronal pathways that terminate axon growth. Accordingly, Lingo-1 may need to form tetramers at the cell surface to have distinct binding sites, relative to the monomer. For example, the signaling complex may consist of four of each binding receptor components (4:4:4) rather than one (1:1:1). Given, however, that Lingo-1 molecules may not necessarily be present as oligomers in the basal state, prior to receptor binding, the mode of Lingo-1 self-interaction observed in the crystal may occur during activation. Lingo-1 appears to be integrated in several central nervous system processes, with the ability to bind multiple signaling molecules, and so its functional roles may vary, and different oligomerization mechanisms may be used in different contexts.

Although the precise arrangement of the inhibitory complex awaits the solution of a crystal structure, the molecular structure of Lingo-1 obtained by the current work can provide useful information about potentially important functional binding sites that can already be integrated into therapeutic discovery programs. Functional validation of these sites should help the design of therapeutic strategies to block signals of axon growth inhibitors and to encourage remyelination.

**Acknowledgements.**—We gratefully acknowledge x-ray resources provided by the Southeast Regional Collaborative Access Team 22-ID beamline at the Advanced Photon Source, Argonne National Laboratory.

## REFERENCES

- He, Z., and Koprivica, V. (2004) *Annu. Rev. Neurosci.* 27, 341–368
- Filbin, M. T. (2003) *Nat. Rev. Neurosci.* 4, 703–713
- Barker, P. A. (2004) *Neuron* 42, 529–533
- Bandtlow, C., and Dechant, G. (2004) *Sci. STKE* 2004, pe 24
- Carim-Todd, L., Escarceller, M., Estvill, X., and Sumoy, L. (2003) *Euro.*

- J. Neurosci.* 18, 3167–3182
6. Mi, S., Lee, X., Shao, Z., Thill, G., Ji, B., Relton, J., Levesque, M., Allaire, N., Perrin, S., Sands, B., Crowell, T., Cate, R. L., McCoy, J. M., and Pepinsky, R. B. (2004) *Nat. Neurosci.* 7, 221–228
  7. Park, J. B., Yiu, G., Kaneko, S., Wang, J., Chang, J., and He, Z. (2005) *Neuron* 45, 345–351
  8. Shao, Z., Browning, J., Lee, X., Scott, M., Shulga-Morskaya, S., Allaire, N., Thill, G., Levesque, M., McCoy, J. M., Murray, B., Jung, V., Pepinsky, R. B., and Mi, S. (2005) *Neuron* 45, 353–359
  9. Mi, S., Miller, R. H., Lee, X., Scott, M. L., Shulga-Morskaya, S., Shao, Z., Chang, J., Thill, G., Levesque, M., Zhang, M., Hession, C., Sah, D., Trapp, B., He, Z., Jung, V., McCoy, J. M., and Pepinsky, R. B. (2005) *Nat. Neurosci.* 8, 745–751
  10. Liang, X., Draghi, N. A., and Resh, M. D. (2004) *J. Neurosci.* 24, 7140–7149
  11. Kotter, M. R., Li, W.-W., Zhao, C., and Franklin, R. J. M. (2006) *J. Neurosci.* 26, 328–332
  12. Zhong, X., Kriz, R., Kumar, R., and Guidotti, G. (2005) *Biochim. Biophys. Acta* 1723, 143–150
  13. Otwinowski, Z., and Minor, W. (1997) *Methods Enzymol.* 276, 307–326
  14. De La Fortelle, E., and Briggone, G. (1997) *Methods Enzymol.* 276, 472–493 (1997)
  15. Cowtan, K. D., and Main, P. (1996) *Acta Crystallogr. Sect. D Biol. Crystallogr.* 52, 43–48
  16. McCoy, A. J., Grosse-Kunstleve, R. W., Storoni, L. C., and Read, R. J. (2005) *Acta Crystallogr. Sect. D Biol. Crystallogr.* 61, 458–464
  17. Emsley, P., and Cowtan, K. (2004) *Acta Crystallogr. Sect. D Biol. Crystallogr.* 60, 2126–2132
  18. Winn, M., Isupov, M., and Murshudov, G. N. (2001) *Acta Crystallogr. Sect. D Biol. Crystallogr.* 57, 122–133
  19. Davis, I. W., Murray, L. W., Richardson, J. S., and Richardson, D. C. (2004) *Nucleic Acids Res.* 32, W615–W619
  20. Yphantis, D., Johnson, M. L., and Lary, J. W. (1997) WinNONLIN program. National Analytical Ultracentrifugation Facility, University of Connecticut, Storrs, CT
  21. Laue, T. M., Shah, B. D., Ridgeway, T. M., and Pelletier, S. L. (1992) in *Analytical Ultracentrifugation in Biochemistry and Polymer Science* (Harding, S. E., Rowe, A. J., and Horton, J. C., eds) pp. 90–125, Royal Society of Chemistry, Cambridge, UK
  22. Pearson, W. R. (1990) *Methods Enzymol.* 183, 63–98
  23. Park, P. S.-H., Filipek, S., Wells, J. W., and Palczewski, K. (2004) *Biochemistry* 43, 15643–15656
  24. He, X. L., Bazan, J. F., McDermott, G., Park, J. B., Wang, K., Tessier-Lavigne, M., He, Z., and Garcia, K. C. (2003) *Neuron* 38, 177–185
  25. Barton, W. A., Liu, B. P., Tzvetkova, D., Jeffrey, P. D., Fournier, A. E., Sah, D., Cate, R., Strittmatter, S. M., and Nikolov, D. B. (2003) *EMBO J.* 22, 3291–3302
  26. Chothia, C., and Jones, E. Y. (1997) *Annu. Rev. Biochem.* 66, 823–862
  27. Casanovas, J. M., Stehle, T., Liu, J. H., Wang, J. H., and Springer, T. A. (1998) *Proc. Natl. Acad. Sci. U.S.A.* 95, 4134–4139
  28. Soroka, V., Kolkova, K., Kastrup, J., Diederichs, K., Breed, J., Kiselyov, V., Poulsen, F., Larsen, L., Welte, W., Berezin, V., Bock, E., and Kasper, C. (2003) *Structure* 11, 1291–1301
  29. Bell, J. K., Mullen, G. E. D., Leifer, C. A., Mazzoni, A., Davies, D. R., and Segal, D. M. (2003) *Trends Immunol.* 24, 528–533
  30. Choe, J., Kelker, M. S., and Wilson, I. A. (2005) *Science* 309, 581–585
  31. Lo Conte, L., Chothia, C., and Janin, J. (1999) *J. Mol. Biol.* 285, 2177–2198
  32. Sharma, S. K., Ramsey, T. M., and Bair, K. W. (2002) *Curr. Med. Chem.* 2, 311–330
  33. Schubert, W. D., Urbanek, C., Ziehlm, T., Beier, V., Machner, M. P., Domann, E., Wehlend, J., Chakraborty, T., and Heinz, D. W. (2002) *Cell* 111, 825–836
  34. Huizinga, E. G., Tsuji, S., Romijn, R. A. P., Shiphost, M. E., deGroot, P. G., Sixma, J. J., and Gros, P. (2002) *Science* 297, 1176–1179
  35. Dumas, J. J., Kumar, R., Seehra, J., Somers, W. S., and Mosyak, L. (2003) *Science* 301, 222–226
  36. Bogan, A. A., and Thorn, K. S. (1998) *J. Mol. Biol.* 280, 1–9
  37. Boggon, T. J., Murray, J., Chappuis-Flament, S., Wong, E., Gumbiner, B. M., and Shapiro, L. (2002) *Science* 296, 1308–1313
  38. Liu, B. P., Fournier, A., GrandPré, T., and Strittmatter, S. M. (2002) *Science* 297, 1190–1193